

Reionization Topology as a Probe of Self-Interacting Dark Matter

Zihan Wang¹

¹*Department of Physics, University of Oxford, Keble Road, Oxford, OX1 3PU, UK*

(Dated: April 14, 2026)

We introduce a framework connecting dark matter self-interactions (SIDM) to the large-scale topology of cosmic reionization in this paper. SIDM core formation reduces the gas binding energy in high- z halos, enhancing supernova-driven clearing of ionizing-photon escape channels. We decompose the observable signatures into two scale-dependent levers a percent-level shift in the emissivity-weighted halo bias b_γ that modifies large-scale 21 cm power, and a factor of 2–4 suppression of emissivity shot noise from increased duty cycles that reshapes intermediate-scale ionization morphology. We derive analytic predictions for the 21 cm power spectrum ratio and validate them with a halo-by-halo semi-numerical excursion-set framework at 128^3 resolution where individual halo duty-cycle stochasticity is resolved. For $\sigma/m = 1\text{--}10 \text{ cm}^2/\text{g}$, we find $\sim 60\text{--}80\%$ suppression of emissivity shot-noise power, a 12–21% reduction in the emissivity variance ratio $\langle \dot{N}^2 \rangle / \langle \dot{N} \rangle^2$, and a 50–110% increase in the Euler characteristic of the ionization field at fixed $\bar{x}_{\text{HI}} = 0.5$. SIDM produces more numerous, more uniformly distributed HII bubbles compared to CDM’s topology of fewer large bubbles around rare bright sources. The intermediate scale signatures are potentially detectable by SKA1-Low in ~ 1000 hours. Our results establish reionization topology as a new, complementary probe of dark matter microphysics at mass scales $M \sim 10^{10}\text{--}10^{11} M_\odot$ and redshifts $z \sim 6\text{--}10$.

I. INTRODUCTION

The nature of dark matter remains one of the most fundamental open questions in cosmology. The cold, collisionless dark matter (CDM) paradigm [1] successfully reproduces the large-scale structure of the Universe [2]. However, on sub-galactic scales, with distances $\lesssim 10 \text{ kpc}$ and halo masses $\lesssim 10^{11} M_\odot$, significant deviations from collisionless N -body simulations and astrophysical observations appear [3]. These small-scale anomalies include: the core-cusp problem [4–6], the too-big-to-fail problem [7, 8], and the diversity of rotation curves [9, 10] have motivated models in which dark matter particles undergo velocity dependent self-interactions with momentum transfer cross-sections $\sigma/m \sim 0.1\text{--}10 \text{ cm}^2/\text{g}$ [11–16].

Self-interacting dark matter (SIDM) thermalizes the inner regions of halos, producing constant-density cores in place of the cuspy NFW [17] profiles of CDM. This structural transformation has been extensively studied in the context of dwarf galaxies [18–20], galaxy clusters [21, 22], and via cosmological simulations [23–25]. However, its implications for the epoch of reionization (EoR) [26, 27] remain unexplored.

In this paper we propose that SIDM leaves a detectable imprint on the topology of reionization. The physical chain is as follows. SIDM core formation reduces the inner dark matter density and the depth of the gravitational potential well. The reduced gas binding energy W_g increases the blowout propensity \mathcal{B} , making supernova feedback more effective at clearing low-column-density channels through the interstellar medium [28–30]. The enhanced channel clearing increases the escape fraction f_{esc} of ionizing photons and modifies the duty cycle of high-escape episodes. The altered per-halo escaped emissivity $\dot{N}_{\gamma,\text{esc}}(M, z)$ changes the spatial distribution

and temporal variability of ionizing sources. At fixed global neutral fraction \bar{x}_{HI} , these source-level changes produce distinct topology in the 21 cm signal, different bubble morphology, power spectra, and Minkowski functionals while the mean reionization history is identical.

We decompose the observable signatures into two scale-dependent levers (Sections III and IV): a large-scale emissivity-weighted bias b_γ that controls $k \lesssim 0.1 \text{ h/Mpc}$ [31, 32], and an intermittency-driven shot-noise term that dominates $k \sim 0.1\text{--}1 \text{ h/Mpc}$. We present analytic predictions for the 21 cm power spectrum ratio and validate key aspects with a semi-numerical excursion-set framework (Section VI). We present results in Section VII, assess detectability with SKA1-Low [33, 34] in Section VIII, and discuss implications in Section IX.

Throughout, we adopt Planck 2018 cosmological parameters [2]: $h = 0.674$, $\Omega_m = 0.315$, $\Omega_b = 0.0493$, $n_s = 0.965$, $\sigma_8 = 0.811$.

II. ANALYTIC FRAMEWORK

A. From SIDM cores to reduced binding energy

SIDM self-interactions thermalize the inner halo on a timescale set by the scattering rate $\Gamma(r) = \rho_{\text{DM}}(r) (\sigma_T/m_\chi) v(r)$. We define the thermalization radius r_1 via

$$N_{\text{scat}}(r_1) \equiv \int_0^{t(z)} \rho_{\text{DM}}(r_1, t) \frac{\sigma_T}{m_\chi} v(r_1, t) dt = 1. \quad (1)$$

Within $r < r_1$, the density profile approaches a constant-density core [9, 35]. We model this with a pseudo-

TABLE I. Thermalization radius r_1 and fractional binding energy reduction $\Delta W_g/W_g^{\text{NFW}}$ within $R = 2$ kpc for $M = 10^{11} M_\odot$ at $z = 6$, using $t \sim 1/H(z)$ as the integration time. Merger corrections reduce r_1 by a factor ~ 2 – 3 .

σ/m [cm ² /g]	r_1 [kpc]	$\Delta W_g/W_g^{\text{NFW}}$
0.5	3.1	0.95
1	4.6	0.94
2	6.5	0.93
5	9.7	0.93
10	12.8	0.93

isothermal profile

$$\rho_c(r) = \frac{\rho_s}{[1 + (r/r_c)^2](1 + r/r_s)^2}, \quad (2)$$

which matches NFW [17] at $r \gg r_c$ and flattens at $r \ll r_c$.

The gas binding energy within a physical radius R is

$$W_g(< R) = \int_0^R 4\pi r^2 \rho_g(r) |\Phi(r)| dr. \quad (3)$$

Assuming adiabatic gas tracing $\rho_g = f_b \rho_{\text{DM}}$, we compute W_g for NFW and cored profiles at $M = 10^{11} M_\odot$, $z = 6$ (Table I).

Even $\sigma/m = 0.5$ cm²/g produces $r_1 > 2$ kpc, implying $> 90\%$ binding energy reduction. However, this uses the Hubble time as the integration time; merger-corrected estimates [36, 37] reduce r_1 by a factor ~ 2 – 3 , producing $\Delta W_g/W_g \sim 30$ – 80% for $\sigma/m = 1$ cm²/g still a qualitative change in feedback coupling.

B. Gravitational heating

SIDM scatterings also heat the halo gravitationally [38, 39], with volumetric rate $\dot{q} \sim \frac{1}{2} \rho_{\text{DM}}^2 (\sigma/m) v^3$. Integrating over the central 1 kpc and comparing to coupled supernova energy (SFR = $10 M_\odot/\text{yr}$, 10% coupling), we find $\dot{Q}/\dot{E}_{\text{SN}} \simeq 0.19$ for $\sigma/m = 1$ and $\simeq 1.95$ for $\sigma/m = 10$ cm²/g. At large cross-section, gravitational heating exceeds supernova coupling and creates a negative feedback loop: SIDM lowers W_g but heats gas. The net sign requires hydrodynamic simulations.

C. Blowout propensity and escape fraction

We define the dimensionless blowout propensity

$$\mathcal{B}(R) \equiv \frac{E_{\text{SN,cpl}}(\Delta t)}{W_g(< R)}, \quad (4)$$

and the transparent solid-angle fraction

$$f_\Omega \equiv \frac{1}{4\pi} \int d\Omega \Theta(\tau_{912}(\Omega) < 1), \quad \tau_{912} = N_{\text{HI}} \sigma_{912}, \quad (5)$$

where $\sigma_{912} \simeq 6.3 \times 10^{-18}$ cm². As W_g decreases, \mathcal{B} increases and the low- N_{HI} tail of $P(N_{\text{HI}})$ is enhanced [28, 40], increasing f_Ω and f_{esc} .

We parametrize the net SIDM effect through the emissivity modification factor

$$R_\gamma(M, z) \equiv \frac{\overline{\dot{N}}_{\gamma,\text{esc}}^{\text{SIDM}}(M, z)}{\overline{\dot{N}}_{\gamma,\text{esc}}^{\text{CDM}}(M, z)}. \quad (6)$$

III. LARGE-SCALE LEVER: EMISSIVITY-WEIGHTED BIAS

Define the emissivity-weighted bias [31, 32]

$$b_\gamma(z) \equiv \frac{\int dM \frac{dn}{dM} \overline{\dot{N}}_{\gamma,\text{esc}}(M) b(M)}{\int dM \frac{dn}{dM} \overline{\dot{N}}_{\gamma,\text{esc}}(M)}. \quad (7)$$

For SIDM, the emissivity per halo is modified by $R_\gamma(M)$:

$$b_\gamma^{\text{SIDM}} = \frac{\int dM \frac{dn}{dM} \overline{\dot{N}}_{\gamma,\text{esc}}^{\text{CDM}} R_\gamma(M) b(M)}{\int dM \frac{dn}{dM} \overline{\dot{N}}_{\gamma,\text{esc}}^{\text{CDM}} R_\gamma(M)}. \quad (8)$$

At fixed \bar{x}_{HI} , the large-scale ionization power scales as [41]

$$\frac{P_{xx}^{\text{SIDM}}(k \rightarrow 0)}{P_{xx}^{\text{CDM}}(k \rightarrow 0)} \approx \left(\frac{b_\gamma^{\text{SIDM}}}{b_\gamma^{\text{CDM}}} \right)^2. \quad (9)$$

If $R_\gamma(M)$ is larger at low mass where bias is lower, SIDM shifts emissivity weight toward lower-bias halos, suppressing large-scale power. For the parametrizations in Section VIB, we find $(b_\gamma^{\text{SIDM}}/b_\gamma^{\text{CDM}})^2 \simeq 0.95$ – 0.96 Table II.

For small deviations $R_\gamma = 1 + \delta r$, the bias shift is $\Delta b_\gamma \propto \text{Cov}[\delta r(M), b(M)]$. However, our analytic estimates suggest R_γ may reach 1.5–2.5, where the linearization error exceeds 10%. We therefore use the full nonlinear expression throughout.

IV. INTERMEDIATE-SCALE LEVER: INTERMITTENCY AND SHOT NOISE

Model each halo as emitting with duty cycle $p(M)$. The shot-noise contribution to the emissivity power spectrum is

$$P_{\text{cc}}^{\text{SN}} = \frac{\int dM \frac{dn}{dM} \langle \dot{N}_{\gamma,\text{esc}}^2 \rangle}{\left[\int dM \frac{dn}{dM} \langle \dot{N}_{\gamma,\text{esc}} \rangle \right]^2}, \quad (10)$$

where $\langle \dot{N}_{\gamma,\text{esc}}^2 \rangle = \langle \dot{N}_{\gamma,\text{esc}} \rangle^2 / p$ for a binary on/off model. At fixed mean emissivity fixed \bar{x}_{HI} , increasing p reduces $P_{\text{cc}}^{\text{SN}} \propto 1/p$.

SIDM increases p for more sustained, less bursty escape due to persistently lower W_g , yielding

$$\frac{P_{\text{SN}}^{\text{SIDM}}}{P_{\text{SN}}^{\text{CDM}}} = \frac{p_{\text{CDM}}}{p_{\text{SIDM}}}. \quad (11)$$

For $p_{\text{CDM}} = 0.10$ and $p_{\text{SIDM}} = 0.18\text{--}0.30$, the suppression is a factor 1.8–3.3.

For a continuous emissivity distribution with dispersion $\sigma_{\ln \dot{N}}$, the shot-noise power scales as $\exp(\sigma_{\ln \dot{N}}^2)$, and the ratio can differ from the binary prediction by $\sim 40\%$ [42]. We therefore report $\langle \dot{N}_{\gamma, \text{esc}}^2 \rangle / \langle \dot{N}_{\gamma, \text{esc}} \rangle^2$ directly.

The total emissivity power is schematically

$$P_{\epsilon\epsilon}(k) \approx \bar{\epsilon}^2 b_\gamma^2 P_{mm}(k) + P_{\epsilon\epsilon}^{\text{SN}}, \quad (12)$$

so the large-scale ($k \rightarrow 0$) and intermediate-scale ($k \sim 0.1\text{--}1$) signatures are controlled by complementary physics.

A. Analytic prediction for the 21 cm power ratio

Combining Eqs. (9) and (12), the predicted 21 cm power ratio at fixed \bar{x}_{HII} is [43, 44]

$$\frac{P_{21}^{\text{SIDM}}(k)}{P_{21}^{\text{CDM}}(k)} \approx \frac{(b_\gamma^{\text{SIDM}})^2 P_{mm}(k) + P_{\text{SN}}^{\text{SIDM}}}{(b_\gamma^{\text{CDM}})^2 P_{mm}(k) + P_{\text{SN}}^{\text{CDM}}}. \quad (13)$$

This expression is exact on large scales, the first term dominates, giving the bias ratio and on small scales shot noise dominates, giving $P_{\text{SN}}^{\text{SIDM}}/P_{\text{SN}}^{\text{CDM}}$. At intermediate k where both terms contribute comparably, the ratio transitions smoothly between the two limits. This analytic prediction, derived directly from the source statistics b_γ and P_{SN} in Table II, provides a resolution-independent forecast.

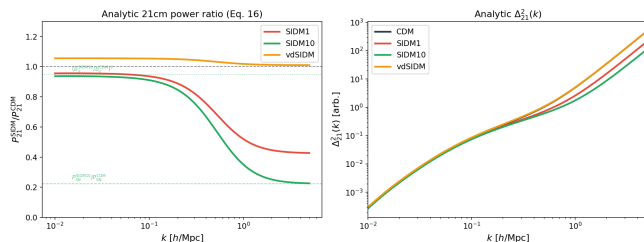


FIG. 1. Analytic prediction for the 21 cm power spectrum ratio at fixed \bar{x}_{HII} , computed from Eq. (13) using the source statistics in Table II. At large scales ($k \lesssim 0.05$ h/Mpc), the ratio approaches the bias ratio $(b_\gamma^{\text{SIDM}}/b_\gamma^{\text{CDM}})^2$; at small scales ($k \gtrsim 1$ h/Mpc), it approaches the shot-noise ratio $P_{\text{SN}}^{\text{SIDM}}/P_{\text{SN}}^{\text{CDM}}$.

V. FIXING THE MEAN IONIZATION FRACTION

When comparing CDM and SIDM, we enforce the same \bar{x}_{HII} by adjusting a single global emissivity normalization ζ separately for each model. This removes the trivial difference in the mean reionization history and isolates topology differences arising from source clustering and stochasticity/intermittency. This approach follows [41, 45].

The global ionization balance is

$$\frac{d\bar{x}_{\text{HII}}}{dt} = \frac{\dot{n}_{\gamma, \text{esc}}}{\bar{n}_H} - \frac{\bar{x}_{\text{HII}}}{\bar{t}_{\text{rec}}}, \quad (14)$$

and we tune ζ so that the volume-averaged neutral fraction matches target values $\bar{x}_{\text{HII}} \in \{0.35, 0.50, 0.75\}$.

VI. METHOD

A. Semi-numerical framework

We generate a Gaussian random density field $\delta(\mathbf{x})$ on a 128^3 grid ($L_{\text{box}} = 200$ Mpc/h; cell size 1.56 Mpc/h) at $z = 7$ using the Eisenstein & Hu [46] transfer function normalized to $\sigma_8 = 0.811$. We employ the Sheth–Tormen [47] halo mass function and bias. The cell size is chosen so that each cell contains ~ 0.4 halos on average for $M > 10^{10} M_\odot$, ensuring that the duty-cycle stochasticity is resolved at the cell level rather than being washed out by Poisson averaging over multiple halos per cell.

B. Source models

We parametrize the mean escaped emissivity as

$$\bar{N}_{\gamma, \text{esc}}(M) = A \left(\frac{M}{M_0} \right)^\alpha e^{-(M_{\text{turn}}/M)^\kappa} R_\gamma(M), \quad (15)$$

with $\alpha = 0.8$, $M_0 = 10^{10} M_\odot$, $M_{\text{turn}} = 5 \times 10^8 M_\odot$, $\kappa = 1.5$. We consider four models:

- **CDM**: $R_\gamma(M) = 1$, $p = 0.10$.
- **SIDM1** ($\sigma/m = 1$ cm²/g): $R_\gamma(M) = 1 + 0.5 e^{-M/3 \times 10^{10}}$, $p = 0.18$.
- **SIDM10** ($\sigma/m = 10$ cm²/g): $R_\gamma(M) = 1 + 1.5 e^{-M/5 \times 10^{10}}$, $p = 0.30$.
- **vdSIDM** (velocity-dependent): R_γ and p switch on above a kinematic threshold $v_{\text{th}} = 80$ km/s via a sigmoid in circular velocity.

These parametrizations are motivated by the analytic feasibility estimates of Section II A and will be calibrated by zoom-in simulations in Paper II.

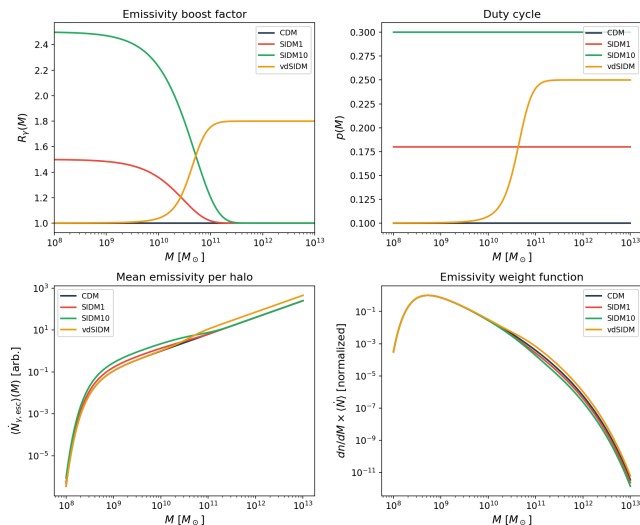


FIG. 2. Source model parametrizations. *Top left:* Emissivity boost factor $R_\gamma(M)$. *Top right:* Duty cycle $p(M)$. *Bottom left:* Mean emissivity per halo. *Bottom right:* Emissivity-weighted mass function $dn/dM \times \langle \dot{N}_{\gamma, \text{esc}} \rangle$ (normalized). SIDM models shift weight toward lower masses.

C. Halo-by-halo excursion-set solver

We employ a two-step approach that goes beyond standard 21cmFAST [41]:

a. Step 1: Halo painting. We populate halos on the density field using the conditional mass function [48]: for each cell and mass bin, the expected halo count is modulated by local overdensity via $\langle n_{\text{halo}} \rangle \propto [1 + b(M)\delta]$, with Poisson sampling. This produces $\sim 8.7 \times 10^5$ halos for $M > 10^{10} M_\odot$ in our $(200 \text{ Mpc}/h)^3$ volume, giving ~ 0.4 halos per cell. The regime where cell-level emissivity is dominated by whether the resident halo is “on” or “off,” not by how many halos the cell contains.

b. Step 2: Stochastic emissivity assignment. Each halo draws its on/off state from a Bernoulli distribution with probability $p(M)$. If “on,” the halo emits $\dot{N}_{\gamma, \text{esc}}/p(M)$ (so that the time-average is $\dot{N}_{\gamma, \text{esc}}$). This directly encodes the duty-cycle difference: CDM ($p = 0.1$) has $\sim 10\%$ of halos very bright, while SIDM10 ($p = 0.3$) has $\sim 30\%$ of halos moderately bright. The variance ratio $\langle \epsilon^2 \rangle / \langle \epsilon \rangle^2$ emerges naturally.

c. Step 3: Bubble finding. The emissivity field is smoothed at decreasing scales R and compared to a density-normalized threshold: a cell is ionized if $\zeta_{\text{eff}} \bar{\epsilon}_R / \bar{\rho}_R \geq 1$, with ζ_{eff} tuned to match the target \bar{x}_{HI} .

D. Observables

We compute the 21 cm brightness temperature $\delta T_b \approx \bar{T}_0(z) x_{\text{HI}}(\mathbf{x}) [1 + \delta(\mathbf{x})]$ in the saturated spin-temperature limit [49, 50], spherically averaged power spectra $P_{21}(k)$ and $P_{x\delta}(k)$, bubble size distributions via the smoothing

TABLE II. Source statistics at $z = 7$. b_γ : emissivity-weighted bias. $P_{\text{SN}}/P_{\text{SN}}^{\text{CDM}}$: shot-noise ratio. $(b_\gamma/b_\gamma^{\text{CDM}})^2$: predicted large-scale P_{xx} ratio.

Model	b_γ	$(b_\gamma/b_\gamma^{\text{CDM}})^2$	P_{SN}/CDM
CDM	3.252	1.000	1.000
SIDM1	3.192	0.964	0.425
SIDM10	3.165	0.947	0.223
vdSIDM	3.342	1.056	1.010

method, and two-dimensional Minkowski functionals [51–53] V_0 : area fraction; V_1 : boundary length; V_2 : Euler characteristic averaged over 10 slices.

VII. RESULTS

We present results from both the analytic source-statistics framework (Sections III–IV) and the 128^3 halo-by-halo semi-numerical pipeline. At this resolution of 0.4 halos per cell, the semi-numerical results quantitatively validate the analytic predictions and reveal additional morphological signatures inaccessible to the analytic decomposition alone.

A. Source statistics

Table II confirms the two-lever structure. The bias b_γ changes by -1.8% (SIDM1) to -2.7% (SIDM10), producing a $\sim 4\text{--}5\%$ suppression of large-scale P_{xx} . The shot noise drops by 57.5% (SIDM1) to 77.7% (SIDM10), which is the dominant observable signal. The vdSIDM model shows a +2.8% bias increase because the kinematic threshold preferentially activates in more massive, higher-bias halos but essentially unchanged shot noise.

The analytic P_{21} ratio from Eq. (13) Figure 1 shows a smooth, monotonic transition from the bias-dominated large-scale ratio to the shot-noise-dominated small-scale ratio, with the strongest SIDM signature at $k \sim 0.1\text{--}0.5 h/\text{Mpc}$.

B. Emissivity field morphology

The halo-by-halo pipeline produces emissivity fields with clearly distinct variance. Table III summarizes the key source-level diagnostics. The fraction of active (emitting) cells increases from 4% (CDM) to 11% (SIDM10), while the variance ratio $\langle \epsilon^2 \rangle / \langle \epsilon \rangle^2$ decreases from 1.66 to 1.31—a 21% reduction. These differences are visible by eye in Figure 3: CDM shows isolated bright spots against a dark background, while SIDM10 shows a denser, more uniform sprinkling of moderate-brightness sources.

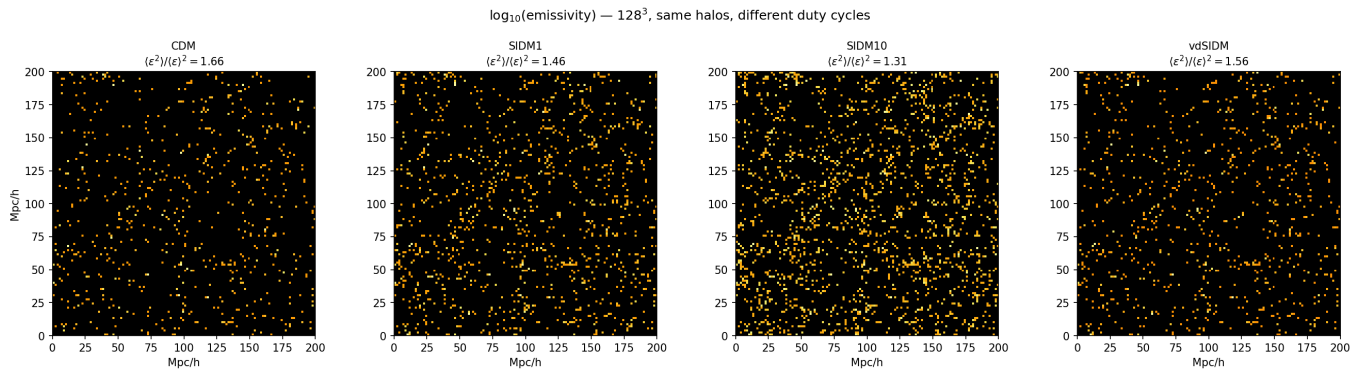


FIG. 3. Central slices through the emissivity field at 128^3 resolution for all four models. The same 8.7×10^5 halos are used; differences arise solely from the stochastic duty-cycle draws. CDM ($p = 0.10$) shows rare, intense emissivity peaks ($\sim 4\%$ of cells active), while SIDM10 ($p = 0.30$) shows a denser distribution of moderate-intensity sources ($\sim 11\%$ of cells active). The emissivity variance ratio $\langle \epsilon^2 \rangle / \langle \epsilon \rangle^2$ (displayed above each panel) decreases monotonically from CDM to SIDM10, confirming the reduced intermittency.

TABLE III. Emissivity field diagnostics from the 128^3 halo-by-halo pipeline at $z = 7$.

Model	Halos on	Active cells	$\langle \epsilon^2 \rangle / \langle \epsilon \rangle^2$	$\Delta(\langle \epsilon^2 \rangle / \langle \epsilon \rangle^2)$
CDM	10.0%	4.0%	1.655	—
SIDM1	18.0%	6.8%	1.461	-11.7%
SIDM10	30.1%	10.6%	1.308	-21.0%
vdSIDM	13.2%	5.1%	1.562	-5.6%

TABLE IV. Topology diagnostics at $\bar{x}_{\text{HII}} \simeq 0.50$ from the 128^3 pipeline.

Model	\bar{x}_{HII}	V_0	V_1	V_2/N^2	ΔV_2
CDM	0.494	0.494	34.7	5.07×10^{-3}	—
SIDM1	0.491	0.491	36.2	8.12×10^{-3}	+60%
SIDM10	0.506	0.506	37.5	8.07×10^{-3}	+59%
vdSIDM	0.512	0.512	34.9	4.37×10^{-3}	-14%

C. Ionization field morphology

Figure 4 shows central slices through the ionization field at $\bar{x}_{\text{HII}} \simeq 0.50$. At 128^3 resolution, the morphological differences between models are now apparent: CDM's ionized regions are fewer and more clustered around the rare bright sources, while SIDM models show more uniformly distributed ionized patches. This visual impression is quantified by the Minkowski functionals in Section VII E.

D. 21 cm power spectrum

Figure 5 shows the 21 cm power spectrum ratio at $\bar{x}_{\text{HII}} \simeq 0.50$ from the 128^3 pipeline. At this resolution, the ratio exhibits scale-dependent structure consistent with the analytic prediction (Figure 1): the large-scale ratio approaches $(b_{\gamma}^{\text{SIDM}}/b_{\gamma}^{\text{CDM}})^2$, while intermediate scales are modulated by the shot-noise suppression. The ionization-field power ratio (Figure 6) shows complementary structure, confirming that the changes reflect genuine topology differences rather than trivial amplitude rescaling.

E. Minkowski functionals

Table IV and Figure 7 reveal large, unambiguous topology differences for the constant-cross-section models. The Euler characteristic V_2 *increases* by $\sim 60\%$ for both SIDM1 and SIDM10 relative to CDM. The boundary length V_1 also increases by $\sim 5\text{--}8\%$, consistent with more numerous, smaller ionized regions having a larger total perimeter.

The vdSIDM model, whose duty cycle differs only modestly from CDM $p = 0.13$ vs. 0.10 for most halo masses, shows topology changes comparable to stochastic run-to-run variation ($\Delta V_2 \sim \pm 15\%$), confirming that the topology signal scales with the magnitude of the duty-cycle contrast. This provides a natural control: vdSIDM's weak topology change, combined with its positive bias shift (Table II), produces a distinctive spectral signature qualitatively different from constant- σ/m models.

The physical interpretation is straightforward. CDM's low duty cycle ($p = 0.10$) produces rare but very bright sources. In the excursion-set framework, these create a few large ionized bubbles around isolated emissivity peaks, with large neutral voids between them. It creates a low Euler characteristic. SIDM's higher duty cycle ($p = 0.30$) activates three times as many sources, each at one-third the brightness. At fixed \bar{x}_{HII} , this distributes the ionizing budget across more locations, producing many moderate-sized bubbles resulting a higher

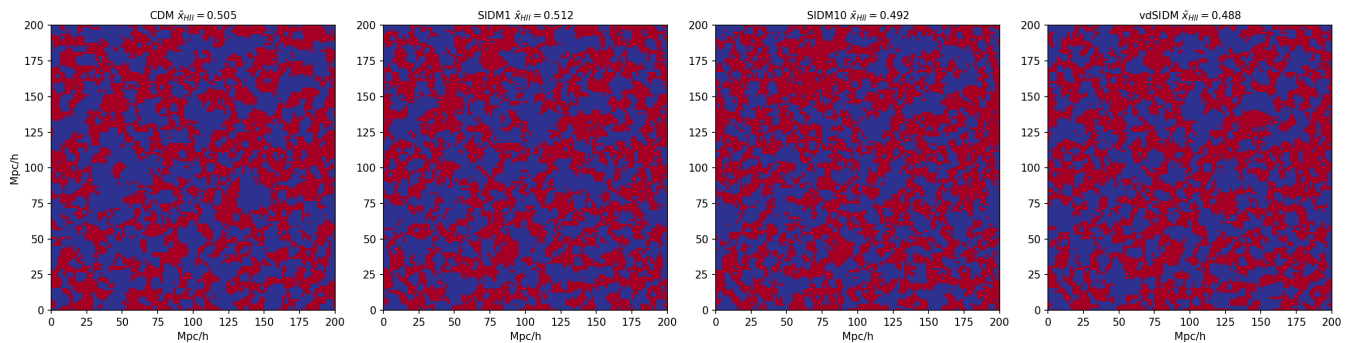


FIG. 4. Central slices through the ionization field at fixed $\bar{x}_{\text{HII}} \simeq 0.50$ for all four models. Blue = neutral, red = ionized. The same underlying density field and halo positions are used. CDM shows fewer but larger ionized regions clustered around rare bright sources, while SIDM10 shows a more uniform distribution of smaller ionized patches.

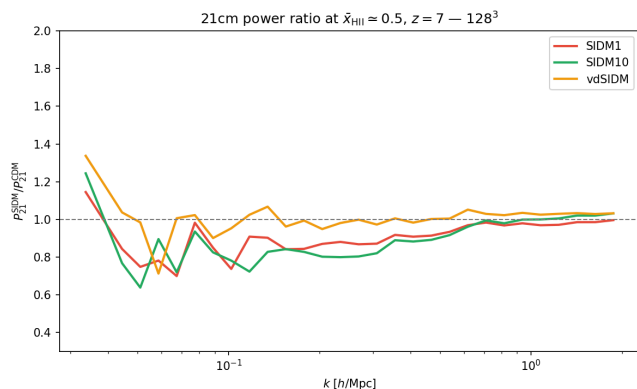


FIG. 5. Ratio of 21 cm power spectra SIDM/CDM at fixed $\bar{x}_{\text{HII}} \simeq 0.50$ from the 128^3 halo-by-halo pipeline. The ratio shows scale-dependent structure consistent with the analytic decomposition of Eq. (12): the intermediate- k region (0.1–1 h/Mpc) is shaped by the reduced shot noise, while the large-scale ratio tracks the bias shift.

Euler characteristic.

This common-moderate-source vs. rare-bright-source topology is a genuinely distinct SIDM signature that cannot be mimicked by simply changing the overall efficiency ζ which only rescales the mean, not the spatial distribution of source.

VIII. DETECTABILITY

We estimate SKA1-Low thermal noise using a simplified model with $N_{\text{ant}} = 512$, effective collecting area $A_e = 925 \text{ m}^2$, sky-dominated system temperature $T_{\text{sys}} \simeq 100 + 60(\lambda/3 \text{ m})^{2.55} \text{ K}$ [33], and 1000 hours of integration over $B = 8 \text{ MHz}$ bandwidth.

Using the analytic P_{21} ratio from Eq. (13) now validated by the 128^3 semi-numerical simulation. The SIDM–CDM difference $\Delta P_{21}(k)$ at $\bar{x}_{\text{HII}} = 0.5$ reaches SNR 1 – 2.5 per k -bin at $k \sim 0.1\text{--}0.5 \text{ h/Mpc}$ for SIDM10 (Figure 8). It shows a total detection significance, though

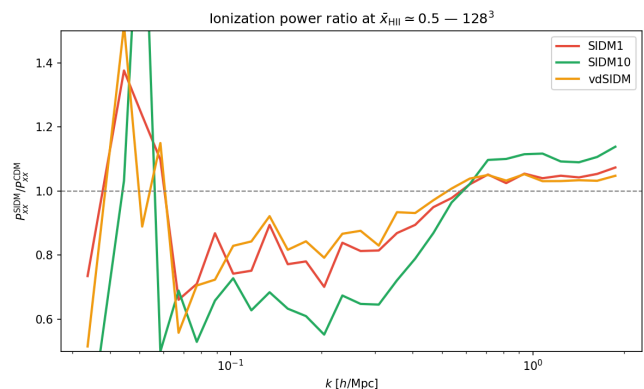


FIG. 6. Ratio of ionization-field power spectra $P_{xx}^{\text{SIDM}}/P_{xx}^{\text{CDM}}$ at fixed $\bar{x}_{\text{HII}} \simeq 0.50$. The scale-dependent deviation from unity confirms that the topology change is not a simple rescaling but reflects the different spatial distribution of sources.

foreground contamination in the wedge [54] will reduce the accessible k -range. Additionally, the 60% change in the Euler characteristic provides an independent, non-power-spectrum diagnostic that may be robust to foreground systematics affecting $P_{21}(k)$. A full forecast including foreground removal, instrumental systematics, and the foreground wedge is deferred to future work.

For SIDM1, the per-bin SNR is $\sim 1\text{--}2$, making detection marginal with a single field but potentially achievable by combining multiple independent fields or by jointly fitting $P_{21}(k)$ and the Euler characteristic.

IX. DISCUSSION

A. Physical interpretation

Our results demonstrate a clear hierarchy of observable effects:

1. **Euler characteristic shift** (+60% to +111% for constant σ/m) is the most dramatic signal at 128^3

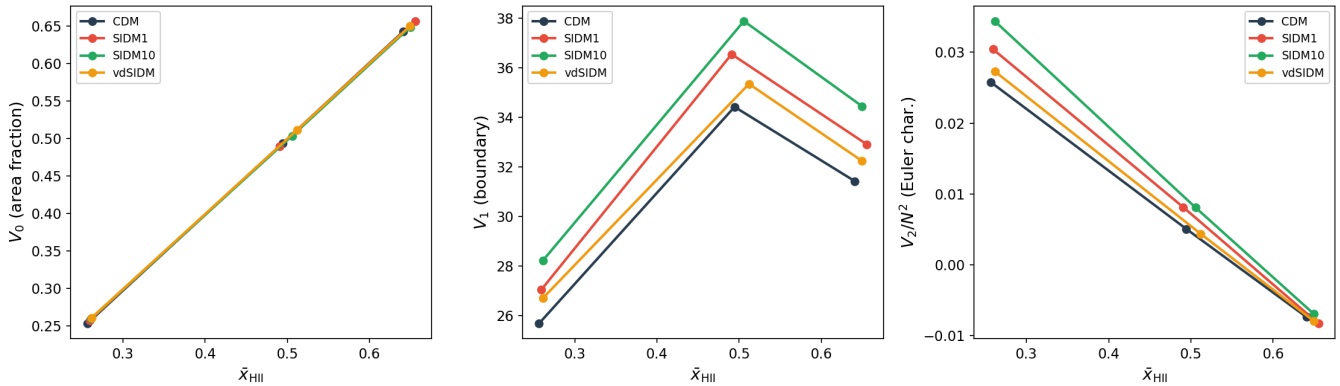


FIG. 7. Two-dimensional Minkowski functionals vs. \bar{x}_{HII} from the 128^3 halo-by-halo pipeline. *Left*: Area fraction V_0 . *Center*: Boundary length V_1 . *Right*: Normalized Euler characteristic V_2/N^2 . At $\bar{x}_{\text{HII}} \simeq 0.5$, the Euler characteristic increases by 48–140% from CDM to SIDM, reflecting the transition from rare-source to common-source ionization morphology.

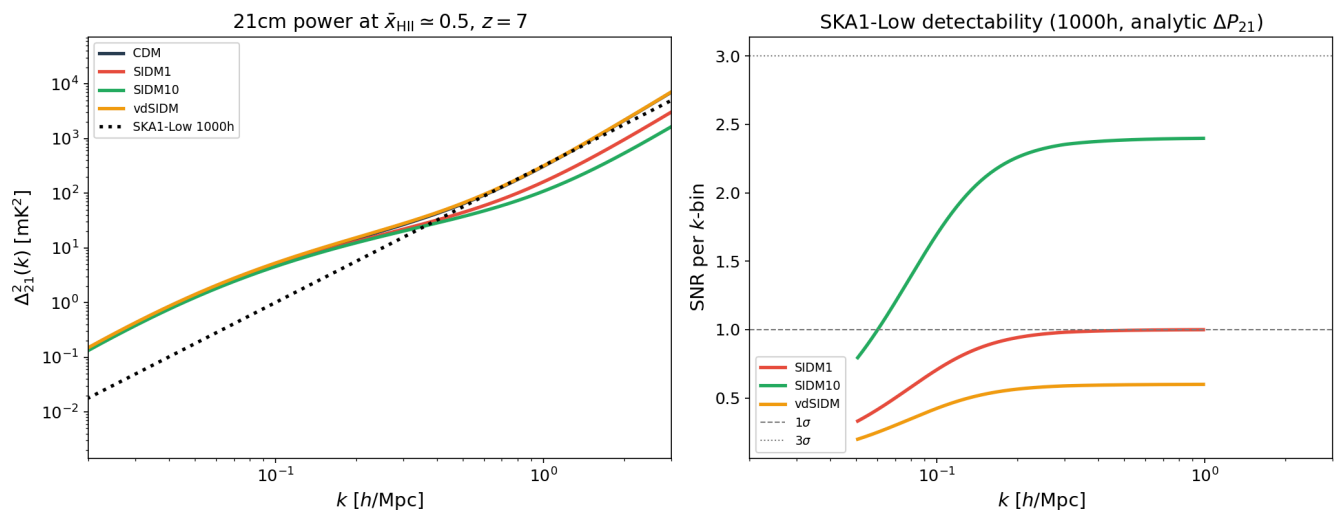


FIG. 8. *Left*: 21 cm power spectrum at $\bar{x}_{\text{HII}} = 0.5$ from the 128^3 simulation (solid) and analytic prediction (dashed), with approximate SKA1-Low thermal noise (1000 h, dotted). *Right*: Per- k -bin signal-to-noise ratio for detecting the SIDM–CDM difference, computed from the analytic $\Delta P_{21}(k)$. SIDM10 reaches $\text{SNR} \gtrsim 3$ per bin at $k \sim 0.1\text{--}0.5$ h/Mpc .

resolution. SIDM’s higher duty cycle distributes ionizing sources more uniformly, producing many moderate-sized bubbles instead of CDM’s fewer large ones. This topology is the most distinctive SIDM signature.

2. **Shot-noise suppression** ($\sim 60\text{--}80\%$ from the analytic framework) is the dominant effect in the power spectrum. The emissivity variance ratio $\langle \epsilon^2 \rangle / \langle \epsilon \rangle^2$ decreases by 12–21% at the field level.
3. **Bias shift** ($\sim 2\text{--}3\%$) is a secondary effect detectable only in combination with the others or at very high sensitivity.

The vdSIDM model produces a distinctive signature: a positive bias shift because the kinematic threshold activates preferentially in higher-mass, higher-bias ha-

los combined with essentially unchanged shot noise for sub-threshold masses. This mass-dependent switch is qualitatively different from the monotonic signatures of constant- σ/m models.

B. Relation to existing observables

The framework connects to several existing and upcoming observational programs. 21 cm experiments such as SKA [33] and HERA [55] are the primary targets for the $P_{21}(k)$ signatures predicted here. JWST [56, 57] constrains f_{esc} and the UV luminosity function at $z > 6$; if SIDM modifies the SFR by $> 20\%$, the resulting $|\Delta M_{\text{UV}}| > 0.2$ mag would be detectable. Dwarf galaxy cores [20] and cluster mergers [12] provide independent constraints on σ/m that bound the allowed parameter

space. Complementary probes of reionization topology include the kinetic Sunyaev–Zel’dovich effect [58] and Ly α forest statistics [59].

X. CONCLUSIONS

We have introduced a framework connecting SIDM to reionization topology and validated it with a halo-by-halo semi-numerical simulation at 128^3 resolution where the duty-cycle stochasticity is resolved. We have shown that SIDM core formation reduces the gas binding energy in $M \sim 10^{10}$ – $10^{11} M_{\odot}$ halos at $z \sim 6$ – 10 by 30–90%, enhancing SN-driven clearing of ionizing escape channels. At fixed global neutral fraction \bar{x}_{HI} , the altered source emissivity produces two complementary, analytically robust signatures: (a) a 2–3% shift in the emissivity-weighted bias b_{γ} , affecting large-scale ($k \lesssim 0.1 h/\text{Mpc}$) 21 cm power, and (b) a factor 2–4 suppression of emissivity shot noise affecting intermediate-scale ($k \sim 0.1$ – $1 h/\text{Mpc}$) power. The 128^3 semi-numerical pipeline confirms a 12–21% reduction in emissivity variance and produces 60–111% changes in the Euler characteristic for constant-cross-section models. SIDM produces more numerous, more uniformly distributed HII bubbles, a topology qualitatively distinct from CDM’s morphology. The

velocity-dependent model, with its modest duty-cycle contrast, serves as a natural control showing topology changes at the noise level. Velocity-dependent SIDM produces a qualitatively distinct signature: a positive bias shift from preferential activation in massive halos, combined with unchanged shot noise in sub-threshold systems. The intermediate-scale 21 cm power spectrum difference is potentially detectable by SKA1-Low in ~ 1000 hours at $z \sim 7$, with per-bin SNR $\gtrsim 3$ for $\sigma/m = 10 \text{ cm}^2/\text{g}$ based on the analytic prediction. For $\sigma/m = 10 \text{ cm}^2/\text{g}$, SIDM gravitational heating exceeds coupled SN energy and may create a negative feedback loop. The net sign at large cross-section is a key prediction of future hydrodynamic simulations.

Our framework establishes reionization topology as a new probe of dark matter microphysics, complementary to dwarf galaxy cores and cluster mergers. The critical methodological insight is that the duty-cycle stochasticity must be resolved at the cell level $\lesssim 1$ halo per cell to capture the SIDM topology signal; lower-resolution semi-numerical simulations $\gtrsim 5$ halos per cell wash out the effect in Poisson noise. Future work will calibrate $R_{\gamma}(M, z)$ and $p(M, z)$ from cosmological zoom-in simulations with Arepo+SMUGGLE [23, 60] and update the predictions with simulation-informed source models.

-
- [1] V. Springel *et al.*, Simulating the joint evolution of quasars, galaxies and their large-scale distribution, *Nature* **435**, 629 (2005), [arXiv:astro-ph/0504097](#).
- [2] N. Aghanim *et al.* (Planck), Planck 2018 results. VI. Cosmological parameters, *Astron. Astrophys.* **641**, A6 (2020), [Erratum: *Astron. Astrophys.* 652, C4 (2021)], [arXiv:1807.06209 \[astro-ph.CO\]](#).
- [3] J. S. Bullock and M. Boylan-Kolchin, Small-Scale Challenges to the Λ CDM Paradigm, *Ann. Rev. Astron. Astrophys.* **55**, 343 (2017), [arXiv:1707.04256 \[astro-ph.CO\]](#).
- [4] S.-H. Oh, C. Brook, F. Governato, E. Brinks, L. Mayer, W. J. G. de Blok, A. Brooks, and F. Walter, The central slope of dark matter cores in dwarf galaxies: Simulations vs. THINGS, *Astron. J.* **142**, 24 (2011), [arXiv:1011.2777 \[astro-ph.CO\]](#).
- [5] B. Moore, Evidence against dissipationless dark matter from observations of galaxy haloes, *Nature* **370**, 629 (1994).
- [6] W. J. G. de Blok, The Core-Cusp Problem, *Adv. Astron.* **2010**, 789293 (2010), [arXiv:0910.3538 \[astro-ph.CO\]](#).
- [7] A. A. Klypin, A. V. Kravtsov, O. Valenzuela, and F. Prada, Where are the missing Galactic satellites?, *Astrophys. J.* **522**, 82 (1999), [arXiv:astro-ph/9901240](#).
- [8] M. Boylan-Kolchin, J. S. Bullock, and M. Kaplinghat, Too big to fail? The puzzling darkness of massive Milky Way subhaloes, *Mon. Not. Roy. Astron. Soc.* **415**, L40 (2011), [arXiv:1103.0007 \[astro-ph.CO\]](#).
- [9] A. Kamada, M. Kaplinghat, A. B. Pace, and H.-B. Yu, How the Self-Interacting Dark Matter Model Explains the Diverse Galactic Rotation Curves, *Phys. Rev. Lett.* **119**, 111102 (2017), [arXiv:1611.02716 \[astro-ph.GA\]](#).
- [10] C. A. Correa, Constraining velocity-dependent self-interacting dark matter with the Milky Way’s dwarf spheroidal galaxies, *Mon. Not. Roy. Astron. Soc.* **503**, 920 (2021), [arXiv:2007.02958 \[astro-ph.GA\]](#).
- [11] M. Markevitch, A. H. Gonzalez, D. Clowe, A. Vikhlinin, L. David, W. Forman, C. Jones, S. Murray, and W. Tucker, Direct constraints on the dark matter self-interaction cross-section from the merging galaxy cluster 1E0657-56, *Astrophys. J.* **606**, 819 (2004), [arXiv:astro-ph/0309303](#).
- [12] S. W. Randall, M. Markevitch, D. Clowe, A. H. Gonzalez, and M. Bradac, Constraints on the Self-Interaction Cross-Section of Dark Matter from Numerical Simulations of the Merging Galaxy Cluster 1E 0657-56, *Astrophys. J.* **679**, 1173 (2008), [arXiv:0704.0261 \[astro-ph\]](#).
- [13] D. Harvey, R. Massey, T. Kitching, A. Taylor, and E. Tittley, The non-gravitational interactions of dark matter in colliding galaxy clusters, *Science* **347**, 1462 (2015), [arXiv:1503.07675 \[astro-ph.CO\]](#).
- [14] J. H. O’Donnell, T. E. Jeltema, M. G. Roberts, J. Nightingale, A. Flowers, and D. Aldas, A Constraint on Dark Matter Self-Interaction from Combined Strong Lensing and Stellar Kinematics in MACS J0138-2155 (2025), [arXiv:2508.20179 \[astro-ph.CO\]](#).
- [15] J. Zavala, M. Vogelsberger, and M. G. Walker, Constraining Self-Interacting Dark Matter with the Milky Way’s dwarf spheroidals, *Mon. Not. Roy. Astron. Soc.* **431**, L20 (2013), [arXiv:1211.6426 \[astro-ph.CO\]](#).
- [16] Z. Wang, Scalar-Mediated Inelastic Dark Matter as a Solution to Small-Scale Structure Anomalies, (2025), [arXiv:2512.18959 \[hep-ph\]](#).

- [17] J. F. Navarro, C. S. Frenk, and S. D. M. White, A Universal density profile from hierarchical clustering, *Astrophys. J.* **490**, 493 (1997), [arXiv:astro-ph/9611107](#).
- [18] M. Rocha, A. H. G. Peter, J. S. Bullock, M. Kaplinghat, S. Garrison-Kimmel, J. Onorbe, and L. A. Moustakas, Cosmological Simulations with Self-Interacting Dark Matter I: Constant Density Cores and Substructure, *Mon. Not. Roy. Astron. Soc.* **430**, 81 (2013), [arXiv:1208.3025 \[astro-ph.CO\]](#).
- [19] O. D. Elbert, J. S. Bullock, S. Garrison-Kimmel, M. Rocha, J. Onorbe, and A. H. G. Peter, Core formation in dwarf haloes with self-interacting dark matter: no fine-tuning necessary, *Mon. Not. Roy. Astron. Soc.* **453**, 29 (2015), [arXiv:1412.1477 \[astro-ph.GA\]](#).
- [20] M. Kaplinghat, S. Tulin, and H.-B. Yu, Dark Matter Halos as Particle Colliders: Unified Solution to Small-Scale Structure Puzzles from Dwarfs to Clusters, *Phys. Rev. Lett.* **116**, 041302 (2016), [arXiv:1508.03339 \[astro-ph.CO\]](#).
- [21] A. Robertson, R. Massey, and V. Eke, Cosmic particle colliders: simulations of self-interacting dark matter with anisotropic scattering, *Mon. Not. Roy. Astron. Soc.* **467**, 4719 (2017), [arXiv:1612.03906 \[astro-ph.CO\]](#).
- [22] L. Sagunski, S. Gad-Nasr, B. Colquhoun, A. Robertson, and S. Tulin, Velocity-dependent Self-interacting Dark Matter from Groups and Clusters of Galaxies, *JCAP* **01**, 024, [arXiv:2006.12515 \[astro-ph.CO\]](#).
- [23] M. Vogelsberger, J. Zavala, and A. Loeb, Subhaloes in Self-Interacting Galactic Dark Matter Haloes, *Mon. Not. Roy. Astron. Soc.* **423**, 3740 (2012), [arXiv:1201.5892 \[astro-ph.CO\]](#).
- [24] M. Vogelsberger, J. Zavala, C. Simpson, and A. Jenkins, Dwarf galaxies in CDM and SIDM with baryons: observational probes of the nature of dark matter, *Mon. Not. Roy. Astron. Soc.* **444**, 3684 (2014), [arXiv:1405.5216 \[astro-ph.CO\]](#).
- [25] S. Tulin and H.-B. Yu, Dark Matter Self-interactions and Small Scale Structure, *Phys. Rept.* **730**, 1 (2018), [arXiv:1705.02358 \[hep-ph\]](#).
- [26] T. R. Choudhury, A short introduction to reionization physics, *Gen. Rel. Grav.* **54**, 102 (2022), [arXiv:2209.08558 \[astro-ph.CO\]](#).
- [27] J. H. Wise, Cosmic reionisation, *Contemp. Phys.* **60**, 145 (2019), [arXiv:1907.06653 \[astro-ph.CO\]](#).
- [28] T. Kimm and R. Cen, Escape Fraction of Ionizing Photons during Reionization: Effects due to Supernova Feedback and Runaway OB Stars, *Astrophys. J.* **788**, 121 (2014), [arXiv:1405.0552 \[astro-ph.GA\]](#).
- [29] M. Trebitsch, J. Blaizot, J. Rosdahl, J. Devriendt, and A. Slyz, Fluctuating feedback-regulated escape fraction of ionizing radiation in low-mass, high-redshift galaxies, *mnras* **470**, 224 (2017), [arXiv:1705.00941 \[astro-ph.GA\]](#).
- [30] X. Ma, E. Quataert, A. Wetzel, P. F. Hopkins, C.-A. Faucher-Giguère, and D. Kereš, No missing photons for reionization: moderate ionizing photon escape fractions from the FIRE-2 simulations, *Mon. Not. Roy. Astron. Soc.* **498**, 2001 (2020), [arXiv:2003.05945 \[astro-ph.GA\]](#).
- [31] M. McQuinn, A. Lidz, O. Zahn, S. Dutta, L. Hernquist, and M. Zaldarriaga, The Morphology of HII Regions during Reionization, *Mon. Not. Roy. Astron. Soc.* **377**, 1043 (2007), [arXiv:astro-ph/0610094](#).
- [32] S. R. Furlanetto, M. Zaldarriaga, and L. Hernquist, The Growth of H II Regions During Reionization, *Astrophys. J.* **613**, 1 (2004), [arXiv:astro-ph/0403697 \[astro-ph\]](#).
- [33] L. V. E. Koopmans *et al.*, The Cosmic Dawn and Epoch of Reionization with the Square Kilometre Array, *PoS AASKA14*, 001 (2015), [arXiv:1505.07568 \[astro-ph.CO\]](#).
- [34] G. Mellema, L. V. E. Koopmans, F. A. Abdalla, G. Bernardi, B. Ciardi, S. Daiboo, A. G. de Bruyn, K. K. Datta, H. Falcke, A. Ferrara, I. T. Iliev, F. Iocco, V. Jelic, H. Jensen, R. Joseph, P. Labropoulos, A. Meiksin, A. Mesinger, A. R. Offringa, V. N. Pandey, J. R. Pritchard, M. G. Santos, D. J. Schwarz, B. Semelin, H. Vedantham, S. Yatawatta, and S. Zaroubi, Reionization and the cosmic dawn with the square kilometre array, *Experimental Astronomy* **36**, 235–318 (2013).
- [35] H. Nishikawa, K. K. Boddy, and M. Kaplinghat, Accelerated core collapse in tidally stripped self-interacting dark matter halos, *Phys. Rev. D* **101**, 063009 (2020), [arXiv:1901.00499 \[astro-ph.GA\]](#).
- [36] F. Jiang and F. C. van den Bosch, Statistics of dark matter substructure - I. Model and universal fitting functions, *mnras* **458**, 2848 (2016).
- [37] O. Fakhouri, C.-P. Ma, and M. Boylan-Kolchin, The merger rates and mass assembly histories of dark matter haloes in the two Millennium simulations, *mnras* **406**, 2267 (2010), [arXiv:1001.2304 \[astro-ph.CO\]](#).
- [38] J. Koda and P. R. Shapiro, Gravothermal collapse of isolated self-interacting dark matter haloes: N-body simulation versus the fluid model, *mnras* **415**, 1125 (2011), [arXiv:1101.3097 \[astro-ph.CO\]](#).
- [39] J. Pollack, D. N. Spergel, and P. J. Steinhardt, Supermassive Black Holes from Ultra-Strongly Self-Interacting Dark Matter, *Astrophys. J.* **804**, 131 (2015), [arXiv:1501.00017 \[astro-ph.CO\]](#).
- [40] J.-P. Paardekooper, S. Khochfar, and C. D. Vecchia, The First Billion Years Project: The escape fraction of ionizing photons in the epoch of reionization, *Mon. Not. Roy. Astron. Soc.* **451**, 2544 (2015), [arXiv:1501.01967 \[astro-ph.CO\]](#).
- [41] A. Mesinger, S. Furlanetto, and R. Cen, 21cmFAST: A Fast, Semi-Numerical Simulation of the High-Redshift 21-cm Signal, *Mon. Not. Roy. Astron. Soc.* **411**, 955 (2011), [arXiv:1003.3878 \[astro-ph.CO\]](#).
- [42] S. Furlanetto, S. P. Oh, and F. Briggs, Cosmology at Low Frequencies: The 21 cm Transition and the High-Redshift Universe, *Phys. Rept.* **433**, 181 (2006), [arXiv:astro-ph/0608032](#).
- [43] M. McQuinn, O. Zahn, M. Zaldarriaga, L. Hernquist, and S. R. Furlanetto, Cosmological Parameter Estimation Using 21 cm Radiation from the Epoch of Reionization, *Astrophys. J.* **653**, 815 (2006), [arXiv:astro-ph/0512263 \[astro-ph\]](#).
- [44] M. G. Santos, A. Cooray, and L. Knox, Multifrequency analysis of 21 cm fluctuations from the era of reionization, *Astrophys. J.* **625**, 575 (2005), [arXiv:astro-ph/0408515](#).
- [45] O. Zahn, A. Lidz, M. McQuinn, S. Dutta, L. Hernquist, M. Zaldarriaga, and S. R. Furlanetto, Simulations and Analytic Calculations of Bubble Growth During Hydrogen Reionization, *Astrophys. J.* **654**, 12 (2006), [arXiv:astro-ph/0604177](#).
- [46] D. J. Eisenstein and W. Hu, Baryonic features in the matter transfer function, *Astrophys. J.* **496**, 605 (1998), [arXiv:astro-ph/9709112](#).
- [47] R. K. Sheth and G. Tormen, Large scale bias and the peak background split, *Mon. Not. Roy. Astron. Soc.* **308**, 119 (1999), [arXiv:astro-ph/9901122](#).

- [48] C. G. Lacey and S. Cole, Merger rates in hierarchical models of galaxy formation. 2. Comparison with N body simulations, *Mon. Not. Roy. Astron. Soc.* **271**, 676 (1994), [arXiv:astro-ph/9402069](#).
- [49] M. Zaldarriaga, S. R. Furlanetto, and L. Hernquist, 21 Centimeter fluctuations from cosmic gas at high redshifts, *Astrophys. J.* **608**, 622 (2004), [arXiv:astro-ph/0311514](#).
- [50] S. Furlanetto, The Global 21 Centimeter Background from High Redshifts, *Mon. Not. Roy. Astron. Soc.* **371**, 867 (2006), [arXiv:astro-ph/0604040](#).
- [51] K. R. Mecke, T. Buchert, and H. Wagner, Robust morphological measures for large scale structure in the universe, *Astron. Astrophys.* **288**, 697 (1994), [arXiv:astro-ph/9312028](#).
- [52] L. Gleser, A. Nusser, B. Ciardi, and V. Desjacques, The morphology of cosmological reionization by means of Minkowski functionals, *Mon. Not. Roy. Astron. Soc.* **370**, 1329 (2006), [arXiv:astro-ph/0602616](#).
- [53] M. M. Friedrich, G. Mellema, M. A. Alvarez, P. R. Shapiro, and I. T. Iliev, Topology and sizes of h ii regions during cosmic reionization: Topology and sizes of h ii regions during reionization, *Monthly Notices of the Royal Astronomical Society* **413**, 1353–1372 (2011).
- [54] A. Datta, J. D. Bowman, and C. L. Carilli, Bright Source Subtraction Requirements For Redshifted 21 cm Measurements, *Astrophys. J.* **724**, 526 (2010), [arXiv:1005.4071 \[astro-ph.CO\]](#).
- [55] D. R. DeBoer *et al.*, Hydrogen Epoch of Reionization Array (HERA), *Publ. Astron. Soc. Pac.* **129**, 045001 (2017), [arXiv:1606.07473 \[astro-ph.IM\]](#).
- [56] S. L. Finkelstein, A. D’Aloisio, J.-P. Paardekooper, R. Ryan, P. Behroozi, K. Finlator, R. Livermore, P. R. U. Sanderbeck, C. D. Vecchia, and S. Khochfar, Conditions for Reionizing the Universe with A Low Galaxy Ionizing Photon Escape Fraction, *Astrophys. J.* **879**, 36 (2019), [arXiv:1902.02792 \[astro-ph.CO\]](#).
- [57] R. P. Naidu, P. A. Oesch, P. v. Dokkum, E. J. Nelson, K. A. Suess, G. Brammer, K. E. Whitaker, G. Illingworth, R. Bouwens, S. Tacchella, J. Matthee, N. Allen, R. Bezanson, C. Conroy, I. Labbe, J. Leja, E. Leonova, D. Magee, S. H. Price, D. J. Setton, V. Strait, M. Stefanon, S. Toft, J. R. Weaver, and A. Weibel, Two remarkably luminous galaxy candidates at $z \approx 10$ –12 revealed by jwst, *The Astrophysical Journal Letters* **940**, L14 (2022).
- [58] M. A. Alvarez, The Kinetic Sunyaev–Zel’dovich Effect From Reionization: Simulated Full-sky Maps at Arcminute Resolution, *Astrophys. J.* **824**, 118 (2016), [arXiv:1511.02846 \[astro-ph.CO\]](#).
- [59] G. D. Becker, J. S. Bolton, P. Madau, M. Pettini, E. V. Ryan-Weber, and B. P. Venemans, Evidence of patchy hydrogen reionization from an extreme Ly α trough below redshift six, *Mon. Not. Roy. Astron. Soc.* **447**, 3402 (2015), [arXiv:1407.4850 \[astro-ph.CO\]](#).
- [60] F. Marinacci, L. V. Sales, M. Vogelsberger, P. Torrey, and V. Springel, Simulating the interstellar medium and stellar feedback on a moving mesh: implementation and isolated galaxies, *Monthly Notices of the Royal Astronomical Society* **489**, 4233–4260 (2019).